Supporting information

Dynamic Monolithic X-ray Imager with Enhanced Performance via Strain Relaxation in Metal-Halide Scintillator

Chongrui Shu[1,2,5], Caixin Zhang[1,5], Ruihan Yuan[1],*, Xixi Liu[3], Shujie Tie[1], Ning Yang[1], Xuan Lian[3], Jianguo Zhu[2],*, Xiaojia Zheng[1,4],*

[1] Institute of Chemical Materials, China Academy of Engineering Physics, Mianyang 621900, Sichuan, China

[2] Department of Materials Science, Sichuan University, Chengdu 610064, China

[3] SensView Technology Co., Ltd., Chengdu 610299, China

[4] Sichuan Research Center of New Materials, Chengdu 610200, China

[5] These authors contributed equally: Chongrui Shu, Caixin Zhang.

*E-mail: xiaojia@caep.cn, yuanruihan17@gscaep.ac.cn, nic0400@scu.edu.cn

KEYWORDS: X-ray imaging, strain, metal-halide, resolution, stability

Materials and methods

Synthesis of Cs$_5$Cu$_3$Cl$_6$I$_2$ powder: Solution-assisted crystallization (SAC) approach: 1.2 mmol of cuprous (I) chloride (CuCl, 99.999%, Alfa), 1.2 mmol of cesium chloride (CsCl, 99.9%, Xi'an p-oled), and 0.8 mmol of cesium iodide (CsI, 99.9%, Xi'an p-oled) raw powders were weighed and added into a 20 mL of glass bottle. Besides, 10 mL of anhydrous acetonitrile (99.8%, Sigma Aldrich) was added, which acted as a crystallization modifier to release strain during chemical reaction. This mixture was stirred for 24 h on a magnetic stirrer for full crystallization of Cs$_5$Cu$_3$Cl$_6$I$_2$. After stirring, the acetonitrile was siphoned by pipette and then the collected precipitates were dried at 40 °C for 2 h to obtain the white SAC-Cs$_5$Cu$_3$Cl$_6$I$_2$ powder.

Hand-grinding method: 1.2 mmol of CuCl, 1.2 mmol of CsCl, and 0.8 mmol of CsI raw powders were added into an agate mortar, and then ground for 2 h to obtain the white ground-Cs$_5$Cu$_3$Cl$_6$I$_2$ powder. It is worth noting that the 2-hour grinding is not continuous but intermittent.

Fabrication of Cs$_5$Cu$_3$Cl$_6$I$_2$ monolithic X-ray imager: The synthesized Cs$_5$Cu$_3$Cl$_6$I$_2$ powder was sifted with a 300-mesh sieve and then mixed with polydimethylsiloxane (PDMS, Sylgard 184, Dow Corning) with the mass ratio of 1:2. After stirring for 20 min, this mixture was placed under vacuum for 15 min to obtain a uniform slurry. A proper amount of the slurry was poured onto CMOS directly and blade-coated to form uniform Cs$_5$Cu$_3$Cl$_6$I$_2$@PDMS scintillation films, followed by annealing at 100 °C for 20 min. Then the monolithic device was obtained. The film thickness can be controlled by varying the height between the blade and CMOS substrate.

Characterizations: The crystal structure of as-explored samples were identified by X-ray diffractometer (Rigaku Ultima IV) with Cu-Kα radiation at a scanning step of 0.02° in 2θ range from 10° to 70°. SEM images were obtained using the scanning electron microscope (Thermo Scientific Apreo 2C). Steady-state photoluminescence (PL) spectra, time-solved PL spectra (TRPL), temperature-dependent PL spectra, and photoluminescence quantum yields (PLQY) were measured on an FLS1000 Photoluminescence Spectrometer, Edinburgh Instruments Ltd (the wavelength of the light source is approximately 300nm). The PL tests employ samples of equivalent

quality (0.1 g). The above characterizations were conducted utilizing powder samples. The photon energy dependent absorption coefficients could be obtained from XCOM database of National Institute of Standards and Technology.

RL measurement and X-ray imaging: Hamamatsu microfocus X-ray source L12161-07 was used as the source of X-rays, which has a minimum X-ray focal spot size of 5 μm. The X-ray source has a diameter of 70 mm. The X-ray dose rate was measured by a Si dosimeter (Fluke, Raysafe X2 R/F), which was calibrated annually by the National Institute of Measurement and Testing Technology. RL spectra were measured by QE-pro spectrometer and an optic-fiber coupled integrating sphere (diameter of 10 mm) in Oceanview system (Ocean Optics). The spectral tests for calculating the light yield utilized a voltage of 50 kV and a current of 50 μA, with the dose rate estimated to be approximately 6 mGy_{air} s^{-1}. Both of the cross-sectional area for $Cs_5Cu_3Cl_6I_2$@PDMS film (2×2 cm^2) and LYSO (circular shape with a diameter of 16 mm) are larger than the hole size of the integrating ball. Besides, the mass concentration of $Cs_5Cu_3Cl_6I_2$ in $Cs_5Cu_3Cl_6I_2$@PDMS films is approximately 33%, whereas LYSO:Ce is pure crystal, and both have a thickness of 370 μm. For detection limit tests, the voltage and current were set at 80 kV and a range of 10 to 80 μA, respectively. The height between the X-ray source and the sample was maintained at 20.1 cm, with a metal plate interposed to attenuate the radiation. The dose rate for these tests spanned from 105 nGy_{air} s^{-1} to 970 nGy_{air} s^{-1}. In the experiments without optical path amplification, the sample is placed in direct contact with the detector, with the X-ray source positioned at a distance of 20 cm from the sample. The bias voltage of the X-ray tube was set at 45 kV and the current was set from 2 μA to 20 μA, and the corresponding dose rate was from 0.8 $μGy_{air}$ s^{-1} to 150 $μGy_{air}$ s^{-1}. In the experiments with optical path amplification, the distance from the X-ray source to the detector is approximately 300 mm, and the distance to the sample is about 70 mm. The X-ray images were recorded with a home-made CMOS detector with an exposure time of 1/18 second. The CsI:Tl and LYSO commercial scintillators were purchased from EPIC Crystal Co., Ltd. The thickness of the scintillators used in imaging tests remained consistent (500 μm).

Calculation of light yield: To calculate the light yield of $Cs_5Cu_3Cl_6I_2$, the commercial scintillator LYSO with known light yield of 33000 photons MeV^{-1} was used as the reference.[1,2] LYSO crystal and $Cs_5Cu_3Cl_6I_2$ film of same size and thickness were placed on the integrating sphere of the Oceanview system, respectively. By comparing the integrated intensity of the RL peak, the light yield of $Cs_5Cu_3Cl_6I_2$ scintillator can be obtained by the following equation:[3]

$$\frac{LY_{Cs_5Cu_3Cl_6I_2}}{LY_{LYSO}} = \frac{\eta_{LYSO}\int I_{Cs_5Cu_3Cl_6I_2}(\lambda)d\lambda \times S_{LYSO}}{\eta_{Cs_5Cu_3Cl_6I_2}\int I_{LYSO}(\lambda)d\lambda \times S_{Cs_5Cu_3Cl_6I_2}} \tag{4}$$

where η represents the X-ray deposited energy percentage of scintillators, S means the radiation area, and I is the RL intensity at different wavelengths (λ). Here, the thickness of LYSO, ground-, and SAC-$Cs_5Cu_3Cl_6I_2$ @PDMS film are 370 μm, respectively. It should be noted that the calculation of light yield is approximate due to the absence of explicit calibration for the light yield of LSYO.

Calculation of Modulation Transfer Function (MTF): The Modulation Transfer function (MTF) is a crucial index to evaluate the spatial resolution performance of imaging system, which represents the transmission capability of the spatial frequency input signal modulation. In this work, the MTF was calculated by the slanted-edge method. Sharp edge X-ray imaging was obtained on the standard tungsten plate. MTF operation on images was processed with software Image J. Then the edge spread function (ESF(x)) was derived from the edge image. The line spread function LSF(x) was the derivation of the ESF(x) and the MTF(v) was the Fourier transform of LSF(x). In summary, the MTF curves can be calculated by the following equation:

$$MTF(v) = F(LSF(x)) = F\left(\frac{dESF(x)}{dx}\right) \tag{5}$$

where v represents the spatial frequency and x means the position of the pixels. The spatial resolution of the scintillator can be evaluated when the MTF value decreases to 0.2.
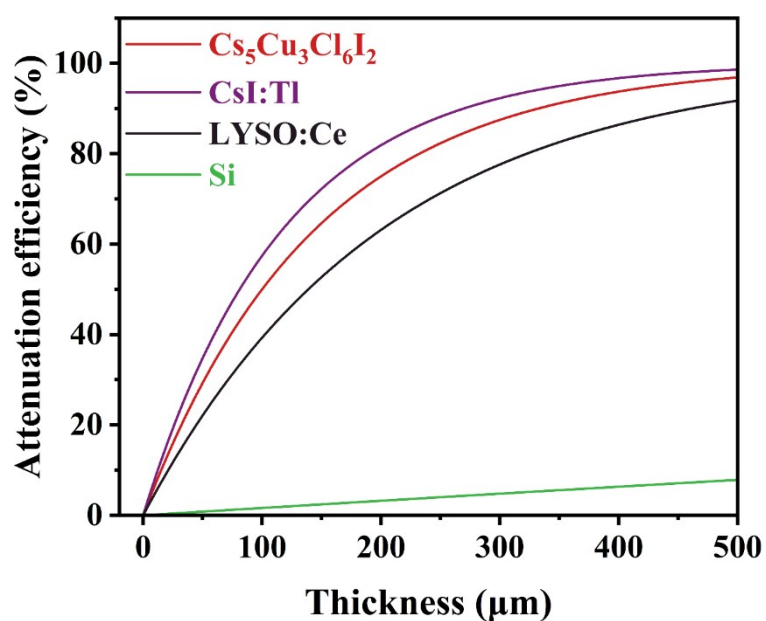
Figure S1. Thickness-dependent attenuation efficiencies of $Cs_5Cu_3Cl_6I_2$, CsI:Tl, LYSO:Ce, and Si to 40 KeV X-ray photons. The X-ray attenuation efficiency (AE) could be obtained from XCOM database of National Institute of Standards and Technology. At same thickness, the X-ray attenuation efficiency of $Cs_5Cu_3Cl_6I_2$ is close to commercial scintillators (CsI:Tl and LYSO:Ce), superior than Si, indicating significant application prospects of $Cs_5Cu_3Cl_6I_2$ in X-ray detection.
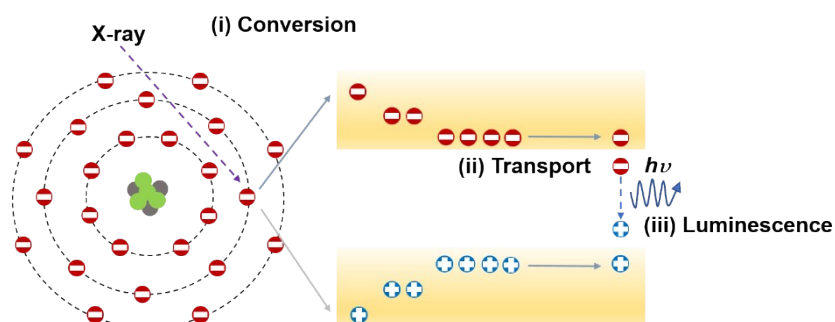
Figure S2. The schematic diagram of radioluminescence mechanism. The RL mechanism of inorganic scintillators can be divided into three main stages (i.e., conversion, transport, and luminescence). During the conversion stage, X-ray radiation interacts with the lattice atoms of scintillators primarily through the photoelectric effect and Compton scattering, resulting in the generation of high-energy electrons and deep holes. Additionally, at energies exceeding 1.02 MeV, pair production also contributes to carrier formation. Subsequently, secondary electrons are generated through electron-electron scattering and Auger processes, leading to the formation of charge carriers with reduced kinetic energy. These carriers then lose energy by interacting with phonons while accumulating at the conduction and valence bands. In the transport stage, electrons and holes migrate towards luminescence centers. However, they may be intercepted by defects or trapped within the crystal lattice, resulting in nonradiative losses and potential delays in radiative recombination. Finally, during the emission process, recombination of charge carriers occurs resulting in visible photon production.
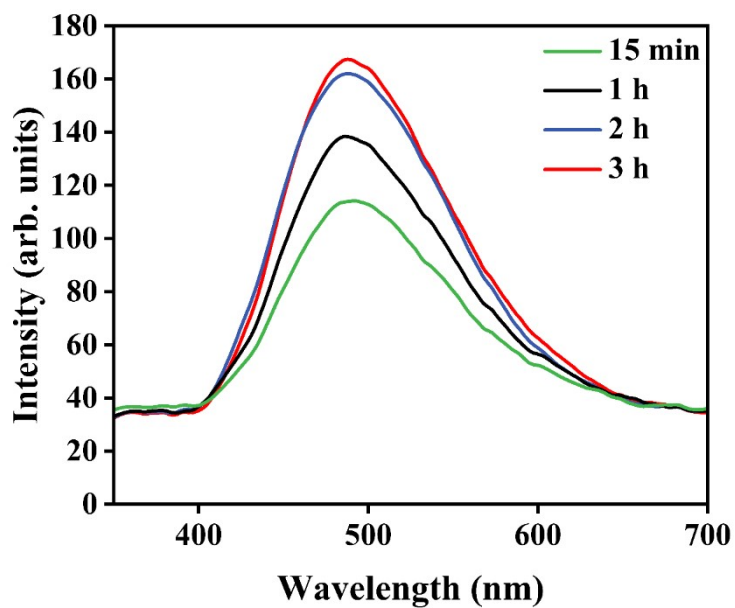
Figure S3. RL spectra of $Cs_5Cu_3Cl_6I_2$ ground for different time (15 min, 1 h,2 h and 3 h). The results indicate that when the grinding time is less than 2 hours, the material exhibits weak luminescence, which may be due to the insufficient reaction of the material. After grinding for 2 hours, the luminescence performance of $Cs_5Cu_3Cl_6I_2$ tends to stabilize and is significantly stronger than that observed with less than 2 hours of grinding. Therefore, we set the grinding time to 2 hours in our experiments.
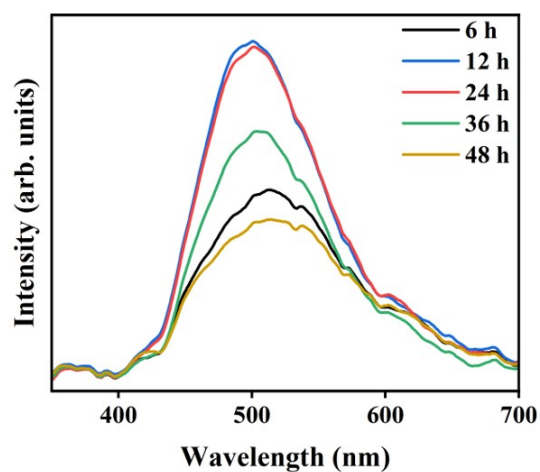
Figure S4. RL spectra of SAC $Cs_5Cu_3Cl_6I_2$ prepared at different reaction times. The RL intensity of samples exhibited an initial increase followed by a subsequent decrease as the SAC time was extended. Notably, the RL intensity of samples at 12 h and 24 h were similar with each other and displayed the highest intensity.
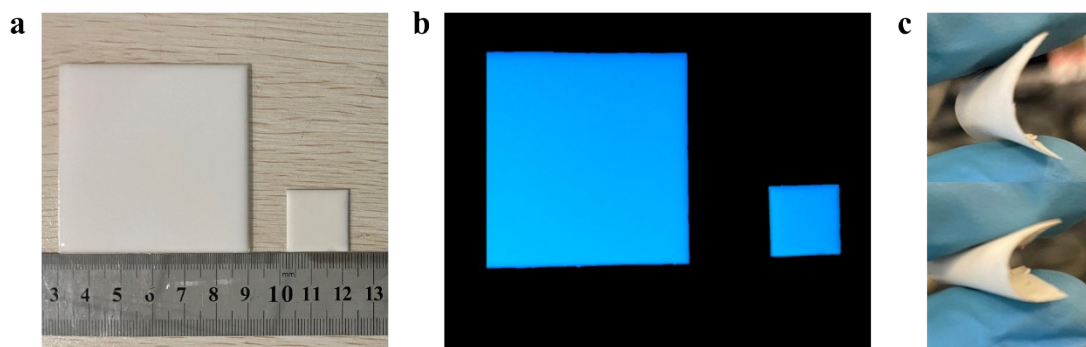
Figure S5. Photographs of (a) $Cs_5Cu_3Cl_6I_2$@PDMS films, (b) blue emission of the films under X-rays, and (c) flexible features of the films. $Cs_5Cu_3Cl_6I_2$@PDMS films could be prepared by blade-coating easily. The thickness and area of the films could be controlled by the height of the blade and the substrate size, respectively. Under X-rays, the $Cs_5Cu_3Cl_6I_2$@PDMS films exhibited excellent blue-emitting properties. Besides, it was a flexible film which could be bent at will without any damages, which are likely to be a commercial scintillator film in the future.
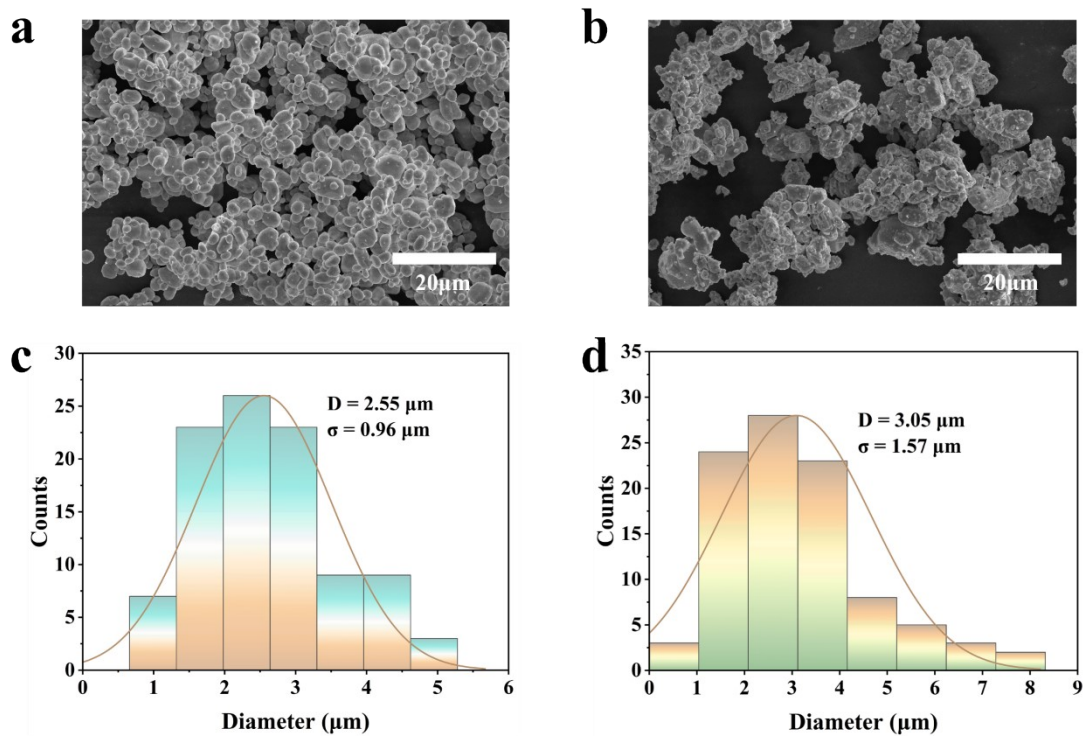
Figure S6. The surface SEM images of (a) SAC- and (b) ground-$Cs_5Cu_3Cl_6I_2$ bulk powder. Size distribution of (c) SAC- and (d) ground-$Cs_5Cu_3Cl_6I_2$ bulk powder extracted from the surface SEM images in Figure 1b, c. About 100 different grains were counted to form this chart. The fitting curve of grain size generally presented a positive distribution trend. The average grain size and standard deviation of SAC-$Cs_5Cu_3Cl_6I_2$ (D = 2.55 μm, σ = 0.96 μm) were smaller than the ground one (D = 3.05 μm, σ = 1.57 μm).
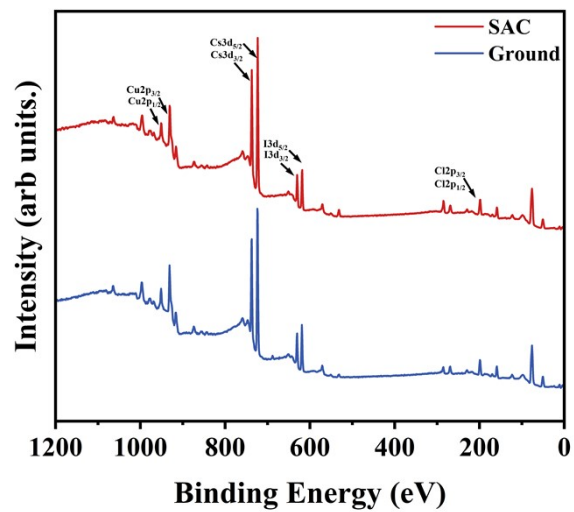
Figure S7. XPS spectra of SAC and Ground-$Cs_5Cu_3Cl_6I_2$.
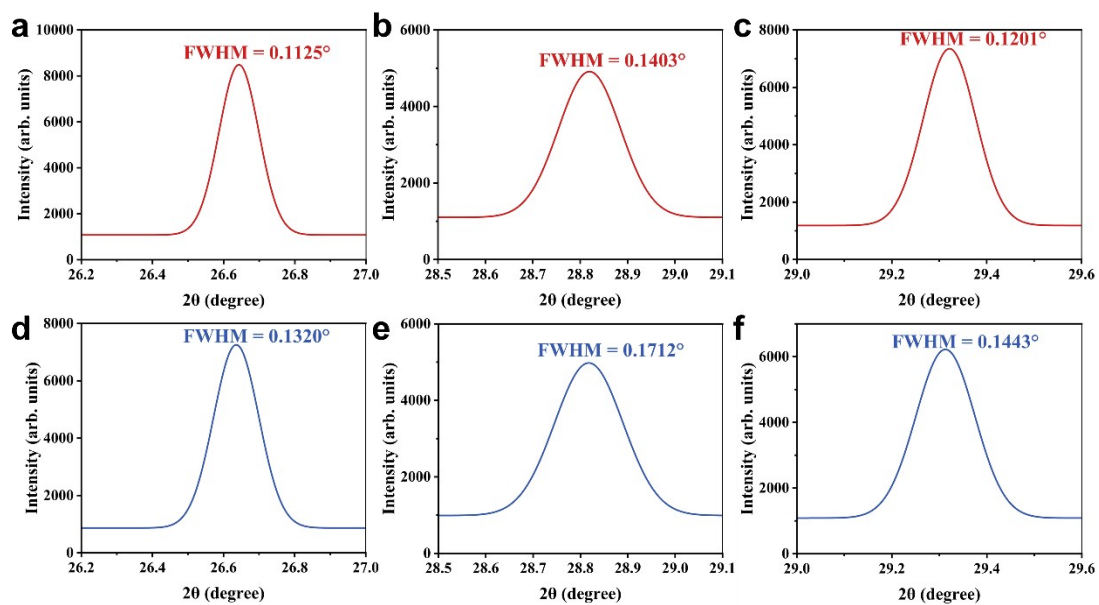
Figure S8. Individual XRD peak of SAC-$Cs_5Cu_3Cl_6I_2$ located at:(a) 26.64°, (b) 28.82°, and (c) 29.32°. Individual XRD peak of ground $Cs_5Cu_3Cl_6I_2$ located at:(d) 26.64°, (e) 28.82°, and (f) 29.32°. The results show that the FWHM of all three peaks for the SAC-$Cs_5Cu_3Cl_6I_2$ are smaller than those for ground-$Cs_5Cu_3Cl_6I_2$.
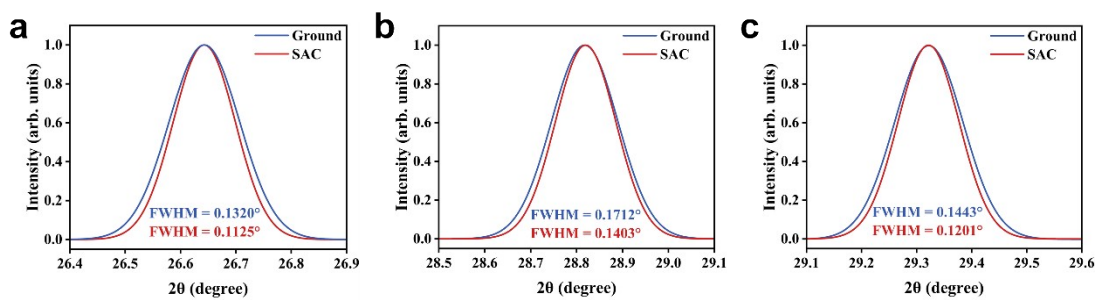
Figure S9. XRD peaks of SAC- and ground $Cs_5Cu_3Cl_6I_2$ located at:(a) 26.64°, (b) 28.82°, and (c) 29.32°. The XRD diffraction peaks in Figure S8 exhibit three prominent XRD peaks, with a noticeable disparity in peak width. This discrepancy can be utilized to demonstrate that SAC generates less strain than the hand ground procedure.
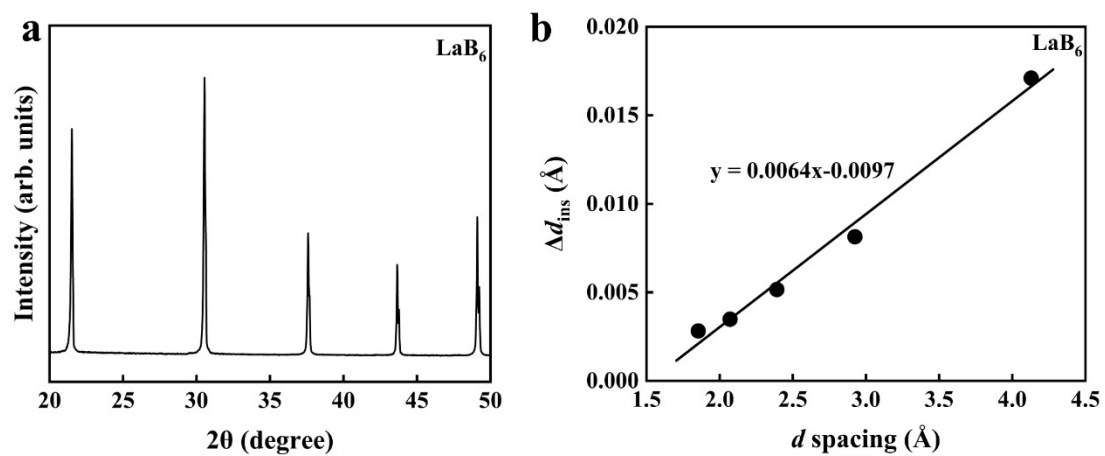
Figure S10. (a) XRD pattern of LaB$_6$; (b) Δd_{inst} versus d spacing extracted from the XRD results. Here, LaB$_6$ was selected as a standard sample because of its standard XRD pattern and line fitting, with a view to calibrating the influence of instrument (Δd_{inst}).
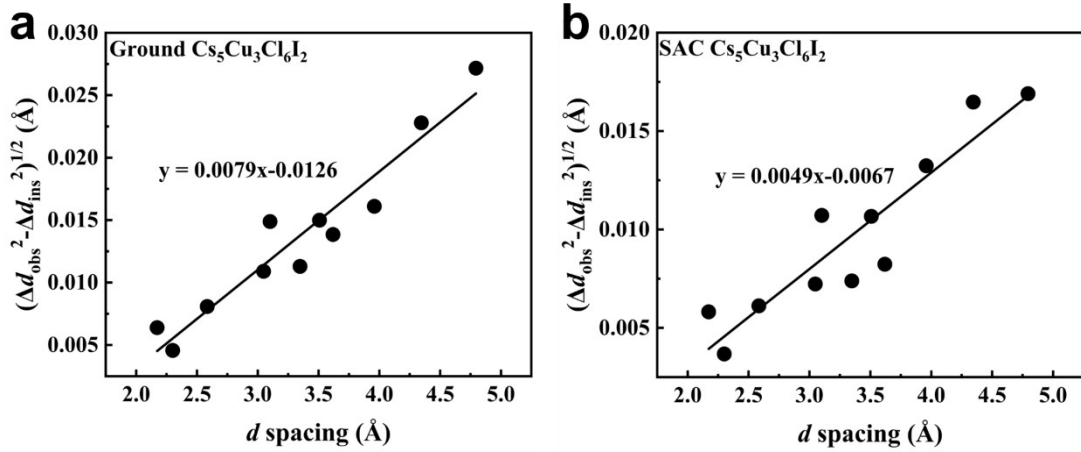
Figure S11. $(\Delta d_{obs}^2 - \Delta d_{inst}^2)^{1/2}$ versus d of the (a) ground $Cs_5Cu_3Cl_6I_2$ and (b) SAC-$Cs_5Cu_3Cl_6I_2$. The Δd slope of the ground sample (0.0079) is greater than that of the SAC sample (0.0049), indicating that the SAC strategy can effectively relieve the lattice strain in $Cs_5Cu_3Cl_6I_2$.
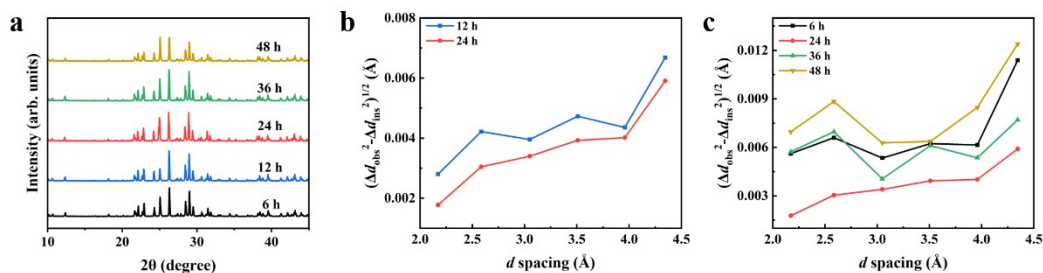
Figure S12. (a) XRD pattern, (b) and (c) strain analysis of SAC $Cs_5Cu_3Cl_6I_2$ samples reacted for different times (6 h, 12 h, 24 h, 36 h, and 48 h).

As shown in Figure S10, the lattice strain for SAC times of 12 h and 24 h are similar, which are lower than samples with SAC time of 6 h, 36 h, and 48 h. There is a clear correspondence between the lattice strain with RL performance (Figure S3), indicating the larger lattice strain result in weaker RL efficiency.

During our experiments, we found that the preparation of $Cs_5Cu_3Cl_6I_2$ in air always resulted in yellow powder samples with poor luminous properties. In previous studies, the yellow $Cs_5Cu_3Cl_6I_2$ was mainly due to the oxidation of I^- to I_2 [4]. In this work, we carry out the experiment in the glove box to obtain white high-quality powder with high reproducibility. However, despite the oxygen content in the glove box being measured ~5 ppm, it was not possible to completely mitigate the influence of oxygen. Thus, excessive SAC time may lead to oxidation and formation of iodine vacancies in the sample, resulting in increased lattice strain and poor scintillation properties. This may explain why the $Cs_5Cu_3Cl_6I_2$ obtained over 24 h exhibits an increase in lattice strain, leading to a decrease in RL performance.
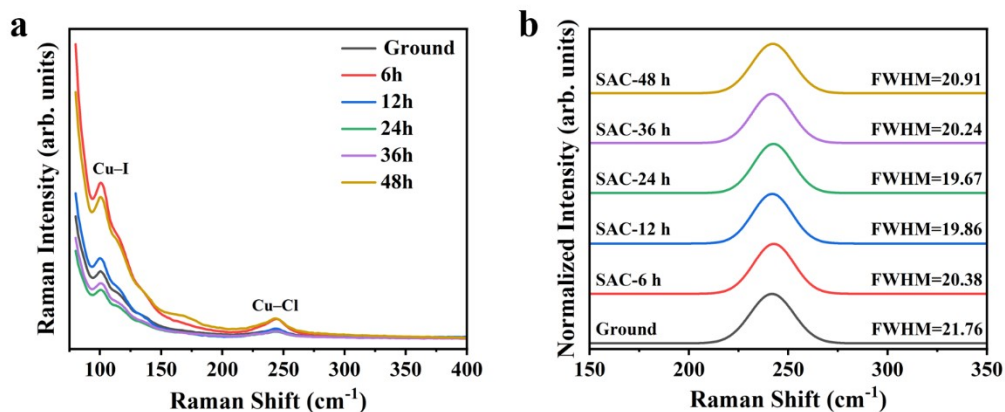
Figure S13. (a) Raman spectra and (b) Gaussian fitting results of the Raman peaks at ~242 cm^{-1} of the Ground-$Cs_5Cu_3Cl_6I_2$ and SAC-$Cs_5Cu_3Cl_6I_2$ with varying reaction times.

As depicted in Figure S11, the lattice strain of $Cs_5Cu_3Cl_6I_2$ was also characterized by Raman spectroscopy. The Raman spectra of Ground-$Cs_5Cu_3Cl_6I_2$ and SAC-$Cs_5Cu_3Cl_6I_2$ with varying reaction times exhibit two peaks at approximately 100 cm^{-1} and 242 cm^{-1}, which can be attributed to the vibrations associated with Cu-I and Cu-Cl bonds, respectively.[4-6] Then, we conducted Gaussian fitting on the peaks at ~242 cm^{-1} to further analyze the Raman results. Remarkably, the SAC-24h sample exhibited the narrowest FWHM (19.67), while conversely, the ground sample displayed the widest FWHM (21.76), indicating that the lattice strain of SAC-24h sample was minimal, whereas that of ground sample was maximal.[7, 8] Moreover, the FWHM of Raman peaks in different reaction times of SAC samples showed a trend of initially decreasing and then increasing, suggesting that lattice strain in SAC samples decreased first and then increased with prolonged reaction time. The above results are consistent with the strain results obtained from XRD analysis (Figure S6-S10).
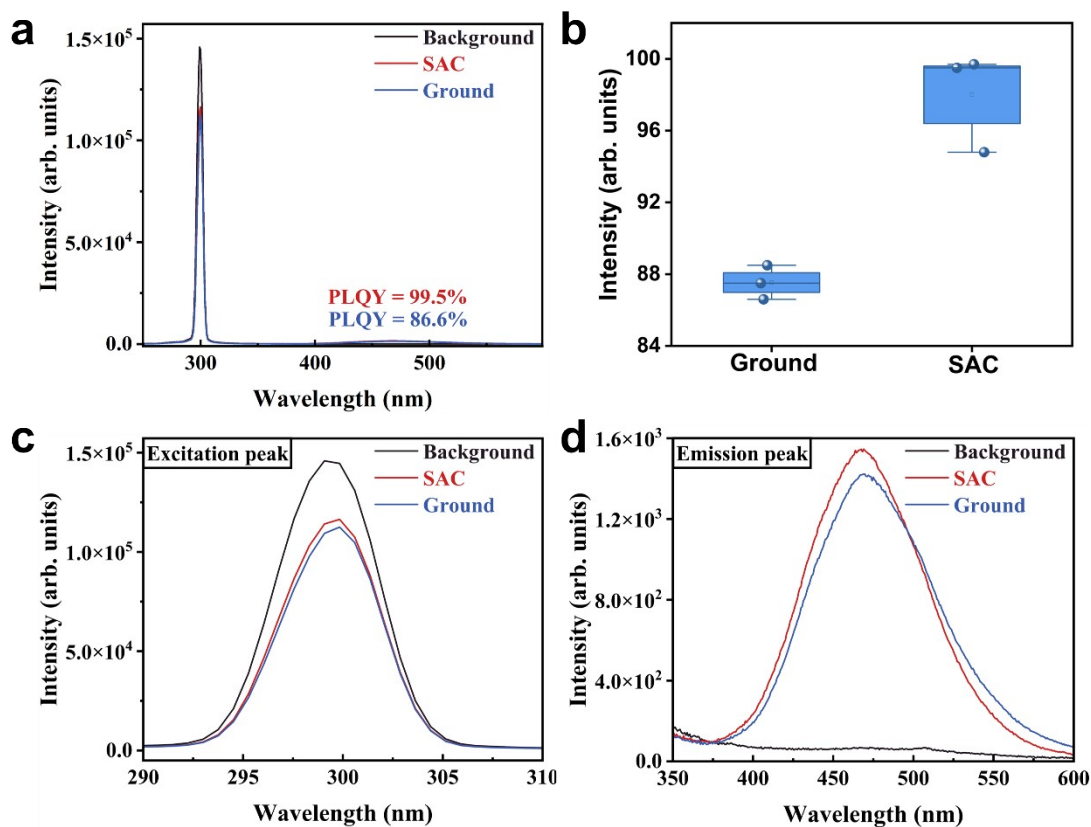
Figure S14. PLQY results of SAC- and ground- $Cs_5Cu_3Cl_6I_2$: (a) original coordinates, (b) PLQY comparison of independent tests, (c) localized amplification of excitation peak and (d) emission peak. The change in the laser peak is not readily discernible due to logarithmic scaling of the ordinate. The coordinates are restored to their initial state, as illustrated in Figure S12a. Besides, three PLQY tests were conducted in our experiment, as shown in Figure S12b. The box plot analysis indicates that the outcomes are statistically reliable within the margin of error. To enhance the visibility of laser peak changes, the image was magnified, as shown in Figure S12c and S12d. The variation of laser peaks becomes evident upon magnification of the image. The observed variation suggests a high accuracy of PLQY tests conducted in our work.
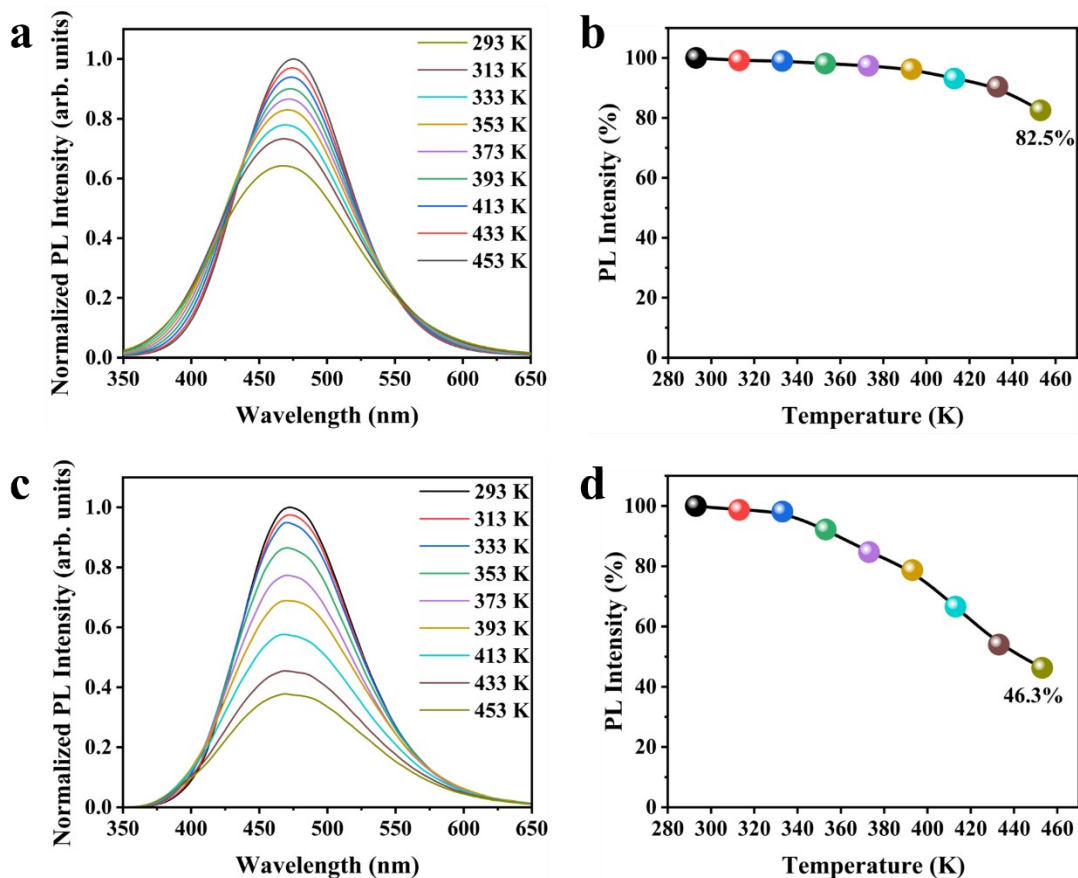
Figure S15. (a) The temperature-dependent PL spectra and (b) corresponding PL emission intensity of SAC-$Cs_5Cu_3Cl_6I_2$; (c) The temperature-dependent PL spectra and (d) corresponding PL emission intensity of ground-$Cs_5Cu_3Cl_6I_2$. The temperature was set from 293 K to 453 K, we recorded the data once every 20 K. With the temperature rising, there was gentle tendency of SAC-$Cs_5Cu_3Cl_6I_2$ before 393 K, and 82.5% of PL emission intensity was retained under a high temperature of 453 K. While the PL intensity of ground-$Cs_5Cu_3Cl_6I_2$ decreased drastically after 333 K which can kept 46.3% of PL emission intensity under 453 K. These results indicate a superior scintillation property of SAC-$Cs_5Cu_3Cl_6I_2$ against heat.
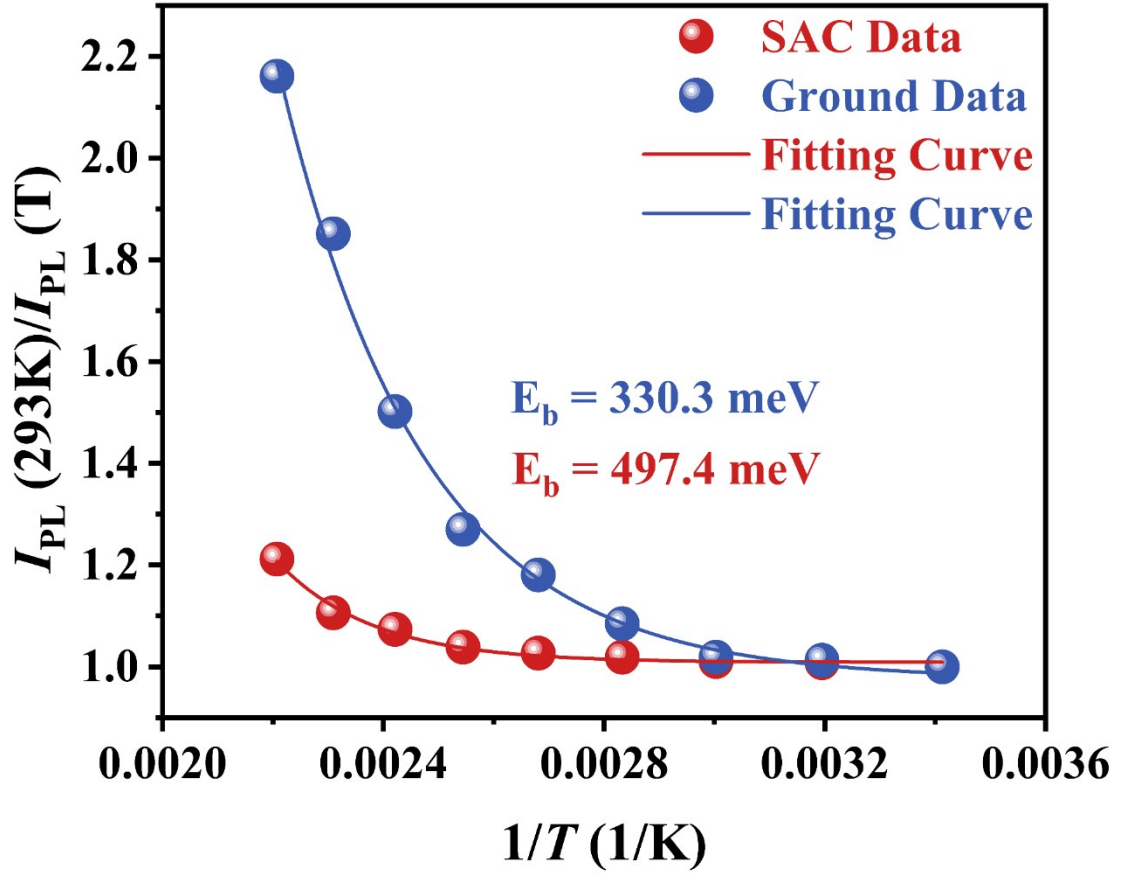
Figure S16. Temperature-dependent PL intensity of the scintillator. The exciton binding energy (E_b) for SAC- and ground-$Cs_5Cu_3Cl_6I_2$ was derived to be 497.4 and 330.3 meV using equation (3) in the main text, respectively. The higher E_b of SAC-$Cs_5Cu_3Cl_6I_2$ indicates a superior thermal stability.
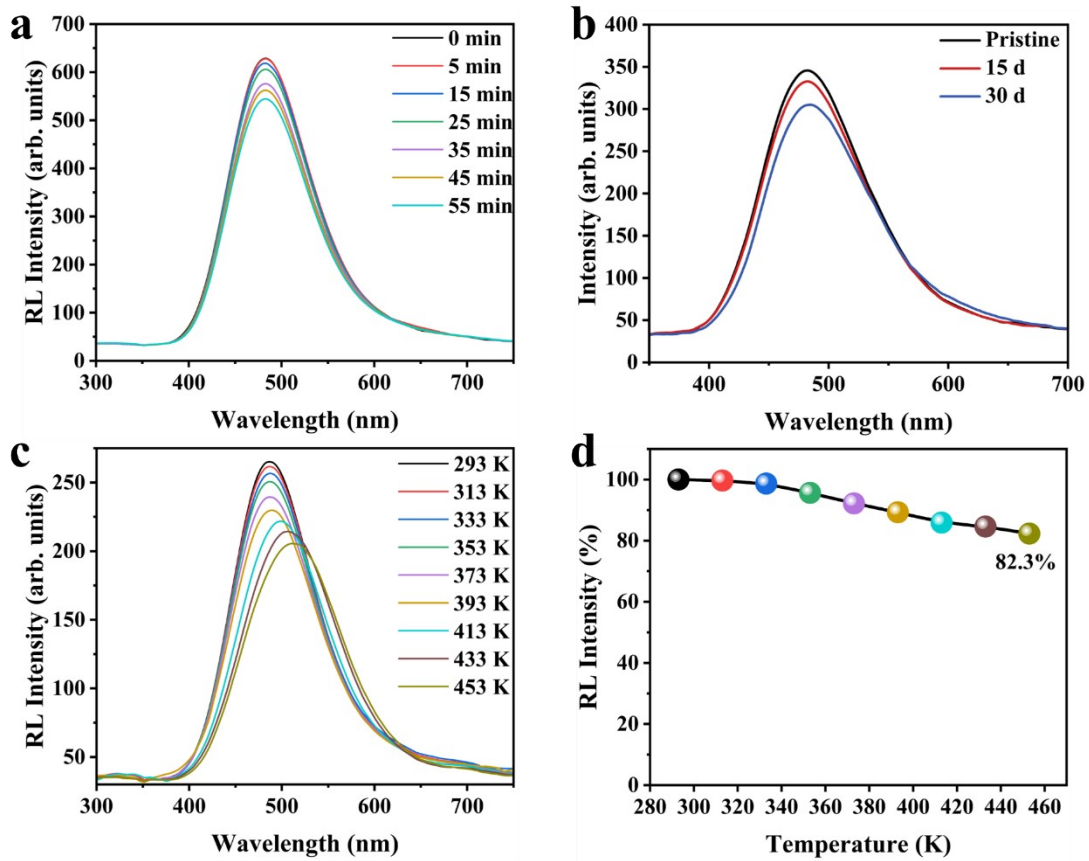
**Figure S17.** (a) RL spectra of SAC-$Cs_5Cu_3Cl_6I_2$@PDMS films placed in water. We put the $Cs_5Cu_3Cl_6I_2$@PDMS film in the water and turned on the X-rays, it exhibited excellent blue-emitting as usual. After 55 min, we took it out of the water, and it remained the excellent scintillation properties. Our $Cs_5Cu_3Cl_6I_2$ encapsulated in PDMS showcases remarkable stability. Immersion in water serves as an extreme condition to assess the material stability. (b) RL spectra of $Cs_5Cu_3Cl_6I_2$ scintillator placed in air for 15 and 30 days. The specific experimental procedure involved placing the $Cs_5Cu_3Cl_6I_2$@PDMS films in humid air (relative humidity of 40%), and subsequently measuring their RL spectra at the 15 d and 30 d intervals. The material maintained over 85% of its initial scintillation properties even after a 30-day exposure, underscoring its exceptional stability. By the way, the humidity stability can be solved by packaging, and will not have much impact on the use of the devices. (c) The temperature-dependent RL spectra of SAC-$Cs_5Cu_3Cl_6I_2$ and (d) corresponding RL emission intensity versus T. The SAC-$Cs_5Cu_3Cl_6I_2$ was heated from 293 K to 453 K on the hot table, and we tested the scintillation properties under the X-ray (dose rate:4.06 mGy_{air} s^{-1}). The RL intensity

decreased slightly with the temperature rising. Even at 453 K, it still possessed remarkable scintillation properties, performing the excellent scintillation property against heat.
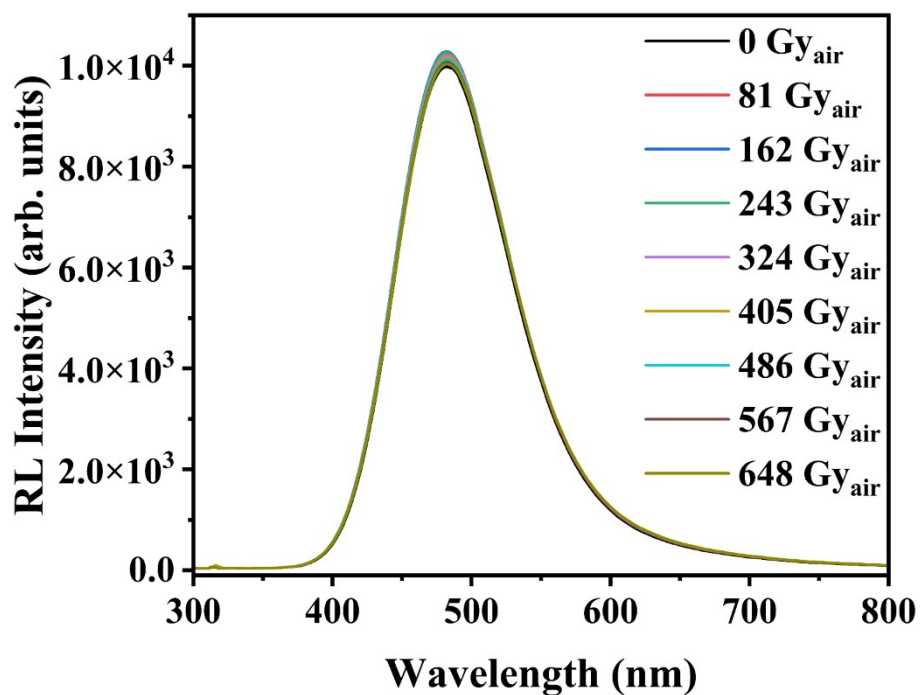
Figure S18. RL spectra of SAC-Cs$_5$Cu$_3$Cl$_6$I$_2$@PDMS films under continuous X-ray irradiation with a dose rate of 45 mGy$_{air}$ s^{-1}. SAC-Cs$_5$Cu$_3$Cl$_6$I$_2$@PDMS film was put under the X-rays and we recorded the data once every 30 min. After an exposure of a total X-ray dose of 648 Gy$_{air}$, there was no obvious decrease in RL intensity, indicating the distinguished stability of our SAC-Cs$_5$Cu$_3$Cl$_6$I$_2$ scintillator under radiation exposure.
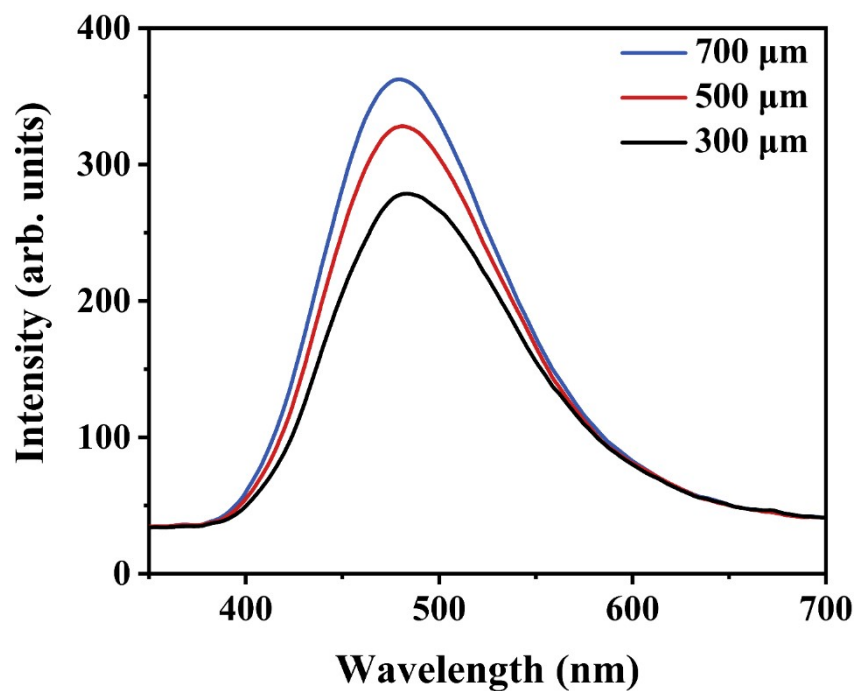
**Figure S19.** RL spectra of different $Cs_5Cu_3Cl_6I_2$ scintillator film. The thickness of the scintillator film can influence PL and RL tests and the resulting imaging outcomes. Here, we further compared the RL spectra of different thicknesses film (300 μm, 500 μm, and 700 μm). The result indicates that as the thickness of the scintillator film increases, the intensity of RL peak also increases.
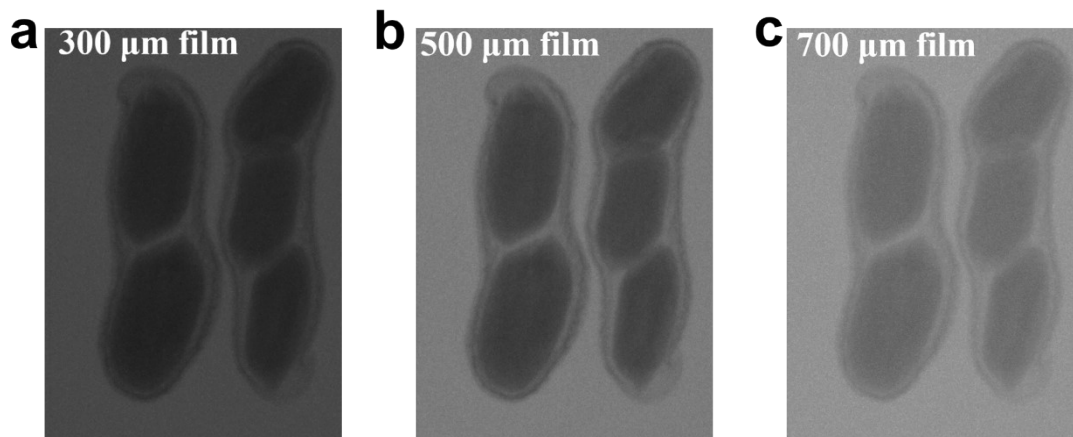
Figure S20. X-ray images of (a) 300 μm, (b) 500 μm, and (c) 700 μm $Cs_5Cu_3Cl_6I_2$ scintillator film. In exploring the impact of scintillator film thickness on imaging results, we compared the imaging performance at different thicknesses (300 μm, 500 μm, and 700 μm). The imaging quality of the low-thickness films (300 and 500 μm) is significantly better than that of the high-thickness ones (700 μm). This is because variations in scintillator thickness can result in different degrees of light scattering, which in turn affects the image quality.
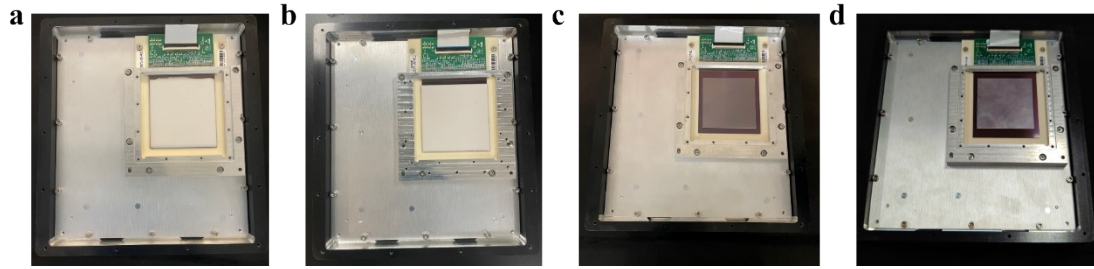
Figure S21. Photographs of (a) monolithic $Cs_5Cu_3Cl_6I_2$@PDMS, and modular (b) $Cs_5Cu_3Cl_6I_2$@PDMS, (c) LYSO:Ce, and (d) CsI:Tl X-ray imaging system. The monolithic imager is fabricated by integrating $Cs_5Cu_3Cl_6I_2$@PDMS and CMOS together, while the modular imager is directly placed $Cs_5Cu_3Cl_6I_2$@PDMS, LYSO:Ce, and CsI:Tl scintillator onto the CMOS scintillator. Different approaches yield distinct imaging outcomes. Our monolithic $Cs_5Cu_3Cl_6I_2$@PDMS imagers exhibit enhanced image distinguishability.
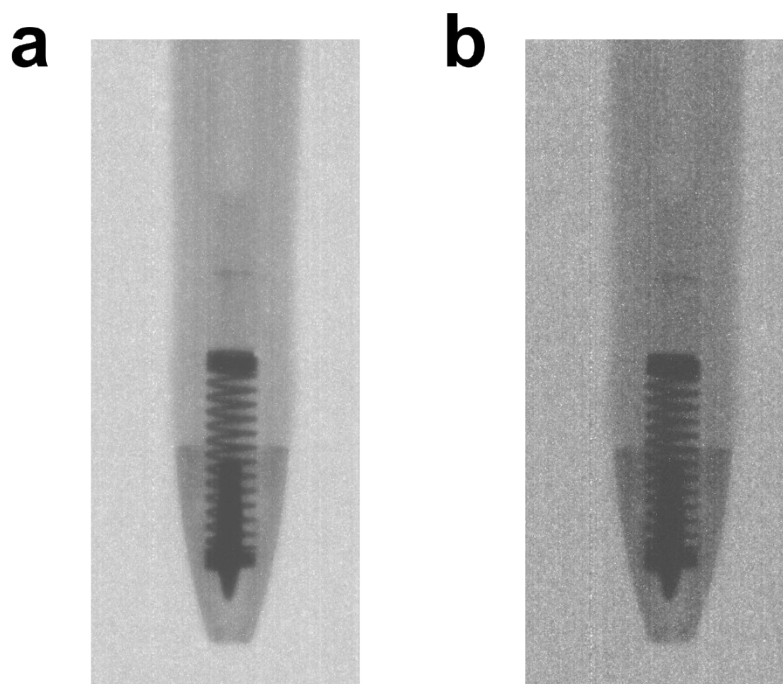
Figure S22. Imaging results of (a) SAC and (b) Ground $Cs_5Cu_3Cl_6I_2$ under an X-ray dose rate of 22 μGy_{air} s^{-1} (45 kV). We investigated X-ray imaging capability of SAC and Ground $Cs_5Cu_3Cl_6I_2$ samples under same CMOS circuit and X-ray radiation condition (45 kV, 5 μA). The thickness of the scintillators used in imaging tests remained consistent (500 μm). At an equivalent dose rate (22 μGy_{air} s^{-1}), the imaging results are depicted in Figure S19. The imaging contrast of samples obtained by SAC is superior to that of ground samples, which implies that SAC samples exhibit a better resolution.

Figure S23. (a) Photographic images of the standard resolution pattern plate. A radiation image resolution card (Type 39b) with 30 lp mm^{-1} was used for the spatial resolution testing.
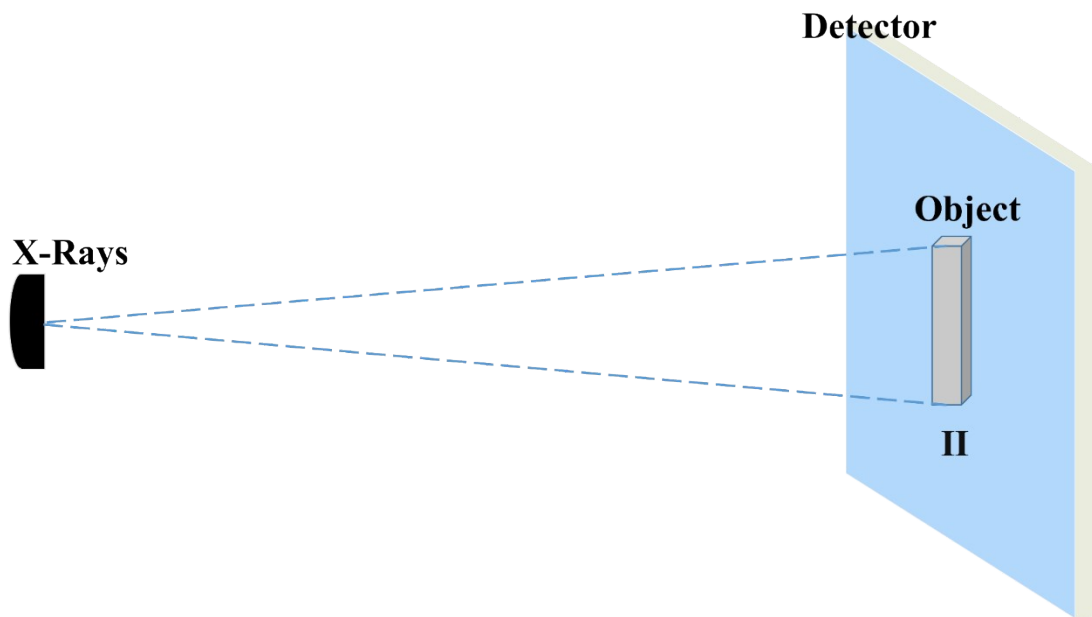
Figure S24. Schematic diagram of operation without optical path amplification.
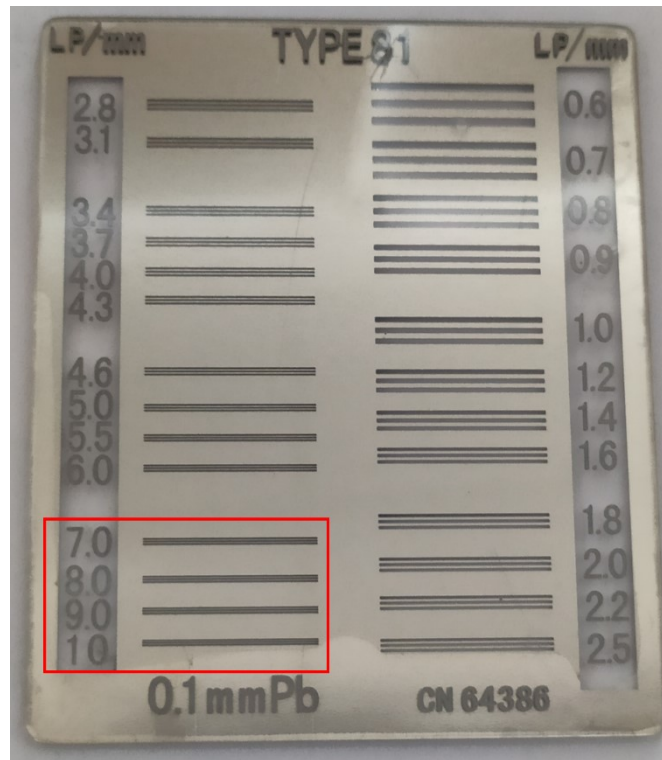
Figure S25. Photographic images of 10 lp mm^{-1} standard resolution pattern plate (Type 81) used for the spatial resolution testing.
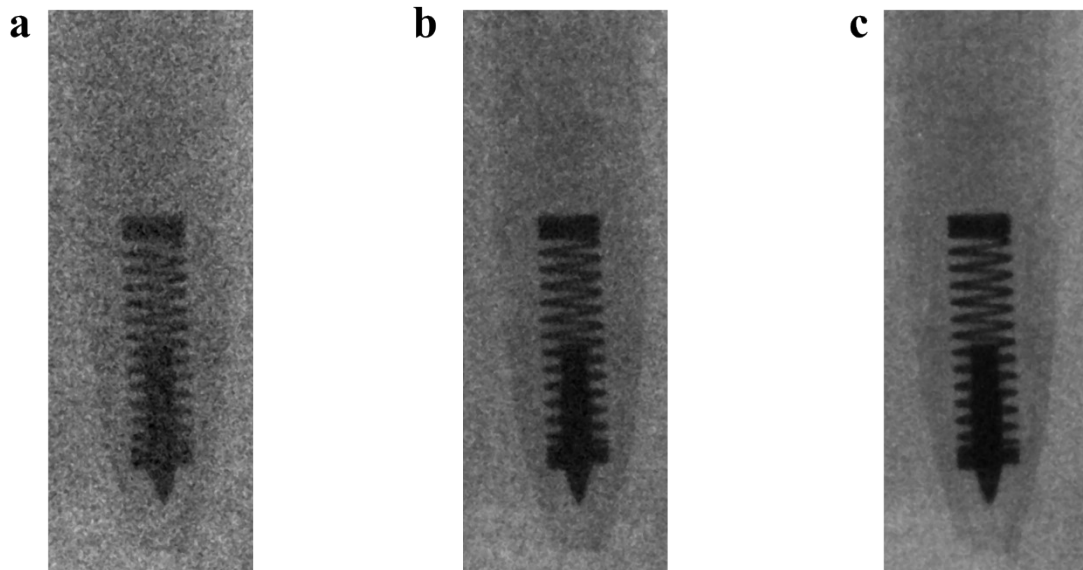
Figure S26. X-ray images of a roller pen under an X-ray dose of (a) 0.8 μGy_{air}, (b) 1.0 μGy_{air}, and (c) 2.3 μGy_{air} from left to right obtained by $Cs_5Cu_3Cl_6I_2$ imager. Even at a low dose of 0.8 μGy_{air}, the details of spring in the roller pen remained distinguishable.

Table S1. Recent research progress of perovskite scintillator X-ray imagers.

Scintillator	Light yield (ph MeV^{-1})	Detection limit (nGy s^{-1})	Spatial resolution (lp mm^{-1})	Spatial resolution (lp mm^{-1} @MTF=0.2)	Directly integrated with image sensor or not	Ref.
Cs$_5$Cu$_3$Cl$_6$I$_2$	**103102**	**34.9**	**＞30.0**	**39.9**	**Yes (CMOS)**	**This work**
Cs$_5$Cu$_3$Cl$_6$I$_2$	57000	71.9	9.0	—	No (Camera)	[9]
Cs$_5$Cu$_3$Cl$_6$I$_2$	59700	60.9	18.0	18.0	No (Camera)	[10]
Cs$_5$Cu$_3$Cl$_6$I$_2$	67200	11.0	＞20.0	27.1	No (Camera)	[11]
Rb$_2$CuBr$_3$	91056	121.5	—	—	—	[12]
Cs$_3$Cu$_2$I$_5$	57000	53.0	12.0	12.0	No (Camera)	[13]
Cs$_3$Cu$_2$I$_5$	48800	48.6	17.0	17.0	No (Camera)	[14]
Cs$_2$AgI$_3$:Cu	82900	77.8	16.2	16.6	No (Camera)	[15]
Rb$_2$CuCl$_3$	16600	88.5	—	—	—	[16]
CsCu$_2$I$_3$	21580	—	5.0	7.5	No (CMOS)	[17]
β-Cs$_3$Cu$_2$Cl$_5$	34000	81.7	—	9.6	No (Camera)	[3]
K$_2$CuBr$_3$	23806	132.8	—	—	—	[18]
Cs$_2$CdBr$_2$Cl$_2$	64950	17.8	—	12.3	No (CMOS)	[19]
CsPbBr$_3$	—	40.1	—	8.0	No (CCD)	[20]
CsPbBr$_3$	40100	—	~15.0	15.0	No (Camera)	[21]
CsPbBr$_3$	15800	120.0	12.5	12.5	No (Camera)	[22]
Cs$_4$PbBr$_6$	19000	2248.0	—	15.9	No (Camera)	[23]
BA$_2$PbBr$_4$:Mn	85000	16.0	10.0	10.7	No (CMOS)	[24]

Table S2. The atomic ratio results of SAC and Ground $Cs_5Cu_3Cl_6I_2$.

	SAC-$Cs_5Cu_3Cl_6I_2$	Ground-$Cs_5Cu_3Cl_6I_2$
Cs	30.34%	31.30%
Cu	29.63%	30.56%
Cl	31.28%	28.13%
I	8.75%	10.01%

Table S3. Fitting results of the TRPL spectra of SAC- and ground-$Cs_5Cu_3Cl_6I_2$ in Figure 2c.

	τ_1	A_1	χ^2
SAC-$Cs_5Cu_3Cl_6I_2$	47.56	1.01	0.99
Ground-$Cs_5Cu_3Cl_6I_2$	41.31	1.01	0.99

References

1. C. Wanarak, W. Chewpraditkul and A. Phunpueok, *Procedia Eng.*, 2012, **32**, 765-771.

2. P. Schotanus and R. Kamermans, *IEEE Trans. Nucl. Sci.*, 1990, **37**, 177-182.

3. Q. Zhou, J. Ren, J. Xiao, L. Lei, F. Liao, H. Di, C. Wang, L. Yang, Q. Chen, X. Yang, Y. Zhao and X. Han, *Nanoscale*, 2021, **13**, 19894-19902.

4. R. Lin, Q. Guo, Q. Zhu, Y. Zhu, W. Zheng and F. Huang, *Adv. Mater.*, 2019, **31**, 1905079.

5. R. Lin, Q. Zhu, Q. Guo, Y. Zhu, W. Zheng and F. Huang, *J. Phys. Chem. C*, 2020, **124**, 20469-20476.

6. L. V. Stepakova, M. Y. Skripkin, L. V. Chernykh, G. L. Starova, L. Hajba, J. Mink and M. Sandström, *J. Raman Spectrosc.*, 2008, **39**, 16-31.

7. B. Jin, J. Cao, R. Yuan, B. Cai, C. Wu and X. Zheng, *Adv. Energy Sustainability Res.*, 2023, **4**, 2200143.

8. Y. Chen, Y. Lei, Y. Li, Y. Yu, J. Cai, M.-H. Chiu, R. Rao, Y. Gu, C. Wang, W. Choi, H. Hu, C. Wang, Y. Li, J. Song, J. Zhang, B. Qi, M. Lin, Z. Zhang, A. E. Islam, B. Maruyama, S. Dayeh, L.-J. Li, K. Yang, Y.-H. Lo and S. Xu, *Nature*, 2020, **577**, 209-215.

9. X. Niu, J. Xiao, B. Lou, Z. Yan, Q. Zhou, T. Lin, C. Ma and X. Han, *Ceram. Int.*, 2022, **48**, 30788-30796.

10. T.-C. Wang, S.-Y. Yao, S.-P. Yan, J. Yu, Z.-Y. Deng, A. N. Yakovlev, B. Meng, J.-B. Qiu and X.-H. Xu, *ACS Appl. Mater. Interfaces*, 2023, **15**, 23421-23428.

11. H. Wu, Q. Wang, A. Zhang, G. Niu, M. Nikl, C. Ming, J. Zhu, Z. Zhou, Y.-Y. Sun, G. Nan, G. Ren, Y. Wu and J. Tang, *Sci. Adv.*, 2023, **9**, eadh1789.

12. B. Yang, L. Yin, G. Niu, J.-H. Yuan, K.-H. Xue, Z. Tan, X.-S. Miao, M. Niu, X. Du, H. Song, E. Lifshitz and J. Tang, *Adv. Mater.*, 2019, **31**, 1904711.

13. T. Chen, X. Li, Y. Wang, F. Lin, R. Liu, W. Zhang, J. Yang, R. Wang, X. Wen, B. Meng, X. Xu and C. Wang, *J. Energy Chem.*, 2023, **79**, 382-389.

14. Y. Zhou, X. Wang, T. He, H. Yang, C. Yang, B. Shao, L. Gutiérrez-Arzaluz, O. M. Bakr, Y. Zhang and O. F. Mohammed, *ACS Energy Lett.*, 2022, **7**, 844-846.

15. T. He, Y. Zhou, P. Yuan, J. Yin, L. Gutiérrez-Arzaluz, S. Chen, J.-X. Wang, S. Thomas, H. N. Alshareef, O. M. Bakr and O. F. Mohammed, *ACS Energy Lett.*, 2023, **8**, 1362-1370.

16. X. Xu, W. Qian, S. Xiao, J. Wang, S. Zheng and S. Yang, *EcoMat*, 2020, **2**, e12064.

17. M. Zhang, J. Zhu, B. Yang, G. Niu, H. Wu, X. Zhao, L. Yin, T. Jin, X. Liang and J. Tang, *Nano Lett.*, 2021, **21**, 1392-1399.

18. W. Gao, G. Niu, L. Yin, B. Yang, J.-H. Yuan, D. Zhang, K.-H. Xue, X. Miao, Q. Hu, X. Du and J. Tang, *ACS Appl. Electron. Mater.*, 2020, **2**, 2242-2249.

19. H. Xu, W. Liang, Z. Zhang, C. Cao, W. Yang, H. Zeng, Z. Lin, D. Zhao and G. Zou, *Adv. Mater.*, 2023, **35**, 2300136.

20. B. Wang, J. Peng, X. Yang, W. Cai, H. Xiao, S. Zhao, Q. Lin and Z. Zang, *Laser Photonics Rev.*, 2022, **16**, 2100736.

21. Y. Zhou, J. Chen, O. M. Bakr and O. F. Mohammed, *ACS Energy Lett.*, 2021, **6**, 739-768.

22. W. Chen, M. Zhou, Y. Liu, X. Yu, C. Pi, Z. Yang, H. Zhang, Z. Liu, T. Wang, J. Qiu, S. F. Yu, Y. Yang and X. Xu, *Adv. Funct. Mater.*, 2022, **32**, 2107424.

23. G. Peng, B. An, H. Chen, Z. Li, Y. Xu, Q. Wang, T. Wang, H. Wang, L. Ding and Z. Jin, *Adv. Opt. Mater.*, 2023, **11**, 2201751.

24. W. Shao, X. Wang, Z. Zhang, J. Huang, Z. Han, S. Pi, Q. Xu, X. Zhang, X. Xia and H. Liang,